(Received 4 September 2024, Accepted 5 November 2024, Scheduled 19 November 2024)

A Large-Frequency-Ratio Filtering Crossover Based on Ridged SIW Resonators

Tianle Zhou[1,2], Yuchen Yin[1,2], Wei Shen[2,*], Zixuan Yi[1,*], and Tao Zhao[2]

[1]School of Communication and Information Engineering, Shanghai University, Shanghai 200444, China
[2]Shanghai Aerospace Institute of Electronic Technology, Shanghai 201109, China

ABSTRACT: A novel filtering crossover featuring flexibly allocated center frequencies based on ridged substrate integrated waveguide (RSIW) is proposed. Two TE_{101}-mode SIW cavities, two loading single ridge SIW (SRSIW) cavities, and a loading triple ridge SIW (TRSIW) cavity are used to realize the filtering crossover. Good transmission and isolation responses can be achieved based on orthogonal degenerate TE_{102} and TE_{201} modes in the centered TRSIW cavity. The frequency ratio of the TE_{102} and TE_{201} modes can be significantly improved by adjusting the aspect ratio and the dimensions of ridges in the centered TRSIW cavity. A prototype operating at 4.98 GHz/10.1 GHz is fabricated and measured. The measured results demonstrate excellent agreement with the simulated one.

1. INTRODUCTION

With the increasing complexity of modern wireless communication systems, planar crossovers have become an integral part of microwave circuits, especially in the development of beamforming networks for multibeam Multiple-Input Multiple-Output (MIMO) antenna systems. Substrate integrated waveguide (SIW) is widely used in various filter designs [1–3], benefiting from its inherent advantages of low cost, low loss, high power handling capability, and high-density integration.

There are many filtering crossovers operating at the same frequency that have been reported previously [4–6]. In [4], a novel SIW filtering crossover with flexibly controlled bandwidth based on orthogonal degenerate TE_{201} and TE_{102} modes in SIW square cavities is proposed. In [5], four TE_{101}-mode cavities are coupled to a square SIW cavity. Substituting the four square cavities with four fundamental mode cavities, the circuit size is reduced by about 35% compared to that in [4]. A new design approach for filtering crossovers featuring dual-band characteristics based on mixed SIW cavities is proposed in [6].

However, with the development of multi-band system applications, two sets of intersecting signals with different operating frequencies are also desired [7–13]. A four-channel filtering crossover with different operating frequencies in two directions is implemented in [7], and by etching a slot on a square SIW cavity, the TE_{102} and TE_{201} modes are split, thus the frequencies can be controlled. In [8], due to employing different TE modes, the frequency ratio of the two passbands can be significantly improved. A wide stopband SIW filtering crossover is proposed in [9], and by controlling the resonant frequencies and mutual couplings of the coupled cavities accordingly, both the center frequencies (CFs) and bandwidths of the two channels can be allocated flexibly. Nevertheless, the conventional SIW filtering crossovers show the disadvantages of large size. There is an urgent need for SIW filtering crossovers with a compact dimension and low loss. A method to achieve miniaturization of SIW is by utilizing ridged SIW (RSIW) technology. A novel compact high-performance filter based on an RSIW resonator and miniaturized half-mode RSIW cavities is proposed in [2], and the effect of loading ridges in the SIW on the resonance frequency of the cavity has been described in detail. This provides excellent theoretical guide for realizing filtering crossover with a large frequency ratio.

In this paper, a filtering crossover with a large frequency ratio of 2.03 is designed by leveraging the effect of the size and position of the ridges on the resonant frequencies of different modes of the RSIW cavity. The reason that variations in the shape and size of a single-ridge lead to change in the resonant frequency of the fundamental mode of a single-ridge SIW cavity is illustrated, as well as the reason that changes in the shape and size of the three-ridge in a triple-ridge SIW cavity lead to changes in the resonant frequencies of TE_{201} and TE_{102}. Due to the application of the harmonic interleaving technique, centered coupling windows, and offset centered feeding ports, the filtering crossover offers a high level of isolation and wide stopband. Good consistency between measurement and simulation proves the practicality of the proposed filtering crossover.

2. ANALYSIS AND DESIGN OF PROPOSED RSIW FILTERING CROSSOVER

2.1. Coupling Scheme

Figure 1(a) depicts the exploded diagram of the proposed RSIW filtering crossover, which is composed of three layers of substrates and three copper layers. The thicknesses of upper and

* Corresponding author: Wei Shen (weishenmw@yeah.net) and Zixuan Yi (yizixuan@shu.edu.cn).

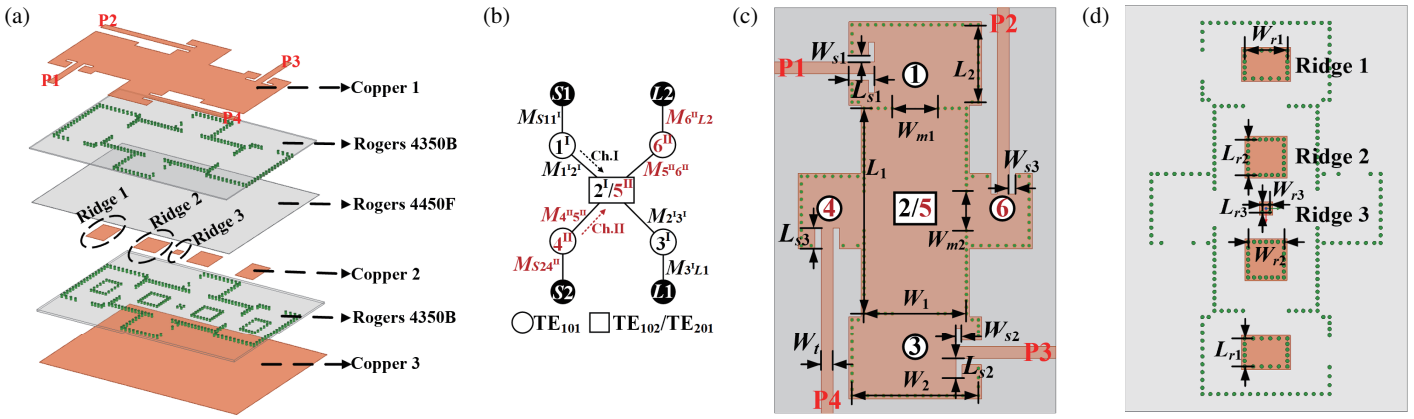

FIGURE 1. Configuration of the proposed filtering crossover. (a) Perspective view. (b) Coupling schematic topology. (c) Upper PCB layer and (d) Lower PCB layer with circuit metal layer.

lower Rogers Duroid 4350B with relative dielectric constant ε_r of 3.48 are 0.254 mm (h_1) and 0.508 mm (h_2), respectively. In addition, two slices of RO4350B are closely stuck by a slice of Rogers Duroid 4450F with a thickness of 0.1 mm and relative dielectric constant ε_r of 3.52. The loss tangent of RO4350B and RO4450F is 0.004. The longitudinal resonators are composed of RSIW cavities. The patches of loaded ridges are embedded in the middle of the lower RO4350B and RO4450F. Five rectangular rings consist of metallized through holes connected to the metal patches on one side and grounded on the other side. All metallic through holes have diameters of 0.6 mm, and the center-to-center pitch between adjacent through holes is 1.2 mm. The coupling windows are placed at the center of the corresponding sidewalls to control the filtering crossover bandwidth. The coupling topology is shown in Fig. 1(b), where the superscripts I and II represent the first and second passbands, respectively.

The proposed SIW filtering crossover centered at 5 GHz and 10.1 GHz within a 20 dB-return loss bandwidth of 170 MHz and 750 MHz is synthesized. The generalized two-port coupling matrix can be obtained by optimization [14]. Moreover, the non-zero elements of the four-port coupling matrix corresponding to channel I are as follows: $M_{S11} = M_{S24} = M_{1S1} = M_{3L1} = M_{4S2} = M_{6L2} = M_{L13} = M_{L26} = 1.0825$, $M_{12} = M_{21} = M_{23} = M_{32} = 1.0303$, $M_{24} = M_{26} = M_{42} = M_{62} = 0.007$. And the non-zero elements of the four-port coupling matrix corresponding to channel II are as follows: $M_{S11} = M_{S24} = M_{1S1} = M_{3L1} = M_{4S2} = M_{6L2} = M_{L13} = M_{L26} = 0.013$, $M_{12} = M_{21} = M_{23} = M_{32} = 1.0303$, $M_{24} = M_{26} = M_{42} = M_{62} = 1.0852$. The relationship between the coupling matrix and S-parameters can be determined by Equations (1a) and (1b).

$$S_{11} = 1 + 2j[A^{-1}]_{1,1}, \quad S_{31} = -2j[A^{-1}]_{8,1} \tag{1a}$$

$$S_{21} = -2j[A^{-1}]_{2,1}, \quad S_{41} = -2j[A^{-1}]_{9,1} \tag{1b}$$

The synthesized and simulated S-parameters are plotted in Fig. 2, which can be seen in good agreement.

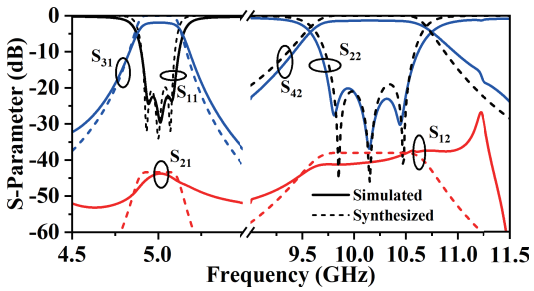

FIGURE 2. Synthesized and simulated near-band frequency responses of the proposed RSIW filtering crossover with different channel CFs.

2.2. Analysis of Loading Single-Ridge SIW Cavity

Figures 3(a) and (b) show a standard square SIW cavity resonator and a loading single-ridge SIW (SRSIW) cavity made of the same material. They are operating at the fundamental mode-TE$_{101}$. For the SIW resonant cavity, the resonant frequency of TE$_{m0q}$ mode can be obtained by [15].

$$f_{TEm0q} = \frac{c}{2\sqrt{\mu_r \varepsilon_r}} \sqrt{\left(\frac{m}{W_{eff}}\right)^2 + \left(\frac{q}{L_{eff}}\right)^2} \tag{2a}$$

$$W_{eff} = W_1 - \frac{d^2}{0.95p}, \quad L_{eff} = L_1 - \frac{d^2}{0.95p} \tag{2b}$$

where c is the light velocity in vacuum. W_1 and L_1 represent the physical length of SIW while W_{eff} and L_{eff} are the width and length of the equivalent rectangular cavity. d is the diameter of the metallized through holes. p is the pitch between the adjacent through holes. μ_r and ε_r represent relative permeability and relative permittivity of the substrate, respectively.

Figures 3(c) and (d) show the equivalent circuits of the standard square SIW cavity and standard square SRSIW cavity, which are proposed in [2]. The standard square SIW cavity resonator can be equivalent to a parallel circuit of a capacitor and an inductor, whose corresponding resonant frequency is:

$$f_{TE101} = f_{r101} = \frac{1}{2\sqrt{LC}} \tag{3a}$$

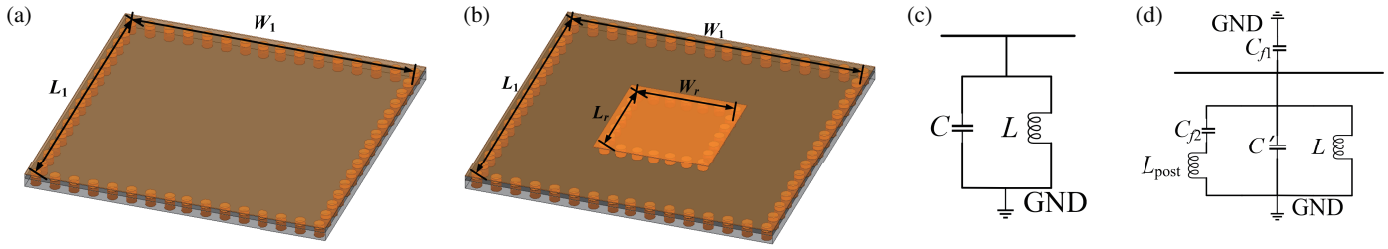

FIGURE 3. (a) The square SIW resonator. (b) The square RSIW resonator. (c) The equivalent circuit of the square SIW resonator. (d) The equivalent circuit of the square RSIW resonator.

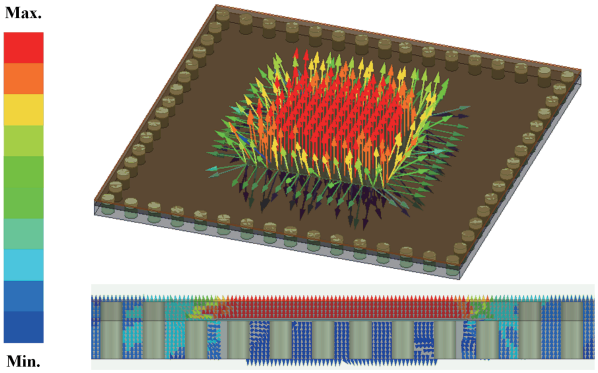

FIGURE 4. Electric field distribution of the fundamental mode in the SRSIW cavity.

$$C = \frac{\varepsilon_r L_{eff}^2}{h} \tag{3b}$$

$$L = \frac{\mu_r h L_{eff}^2}{2c^2\pi^2 L_1} \tag{3c}$$

where h denotes the substrate thickness of the SIW cavity. L_1 denotes the physical length of the square SIW cavity. As shown in Fig. 3(d), the value of C_{f1} and C_{f2} can be driven as

$$C_{f1} = \frac{\varepsilon_r \pi L_r^2}{h_1} \tag{4a}$$

$$C_{f2} = \frac{\varepsilon_r \pi L_r^2}{h_2} \tag{4b}$$

In addition, L_{post} can be denoted as

$$L_{post} \approx \frac{5.08 h_2}{n}\left[\ln\left(\frac{4h_2}{d}\right)\right] \tag{4c}$$

where n denotes the quantity of the metallized through-holes connecting the metal sheet to the ground. C' is the rest capacitance of the cavity. The SRSIW resonator will resonate when the imaginary part of the input admittance in Fig. 3(d) equals 0, as

$$\frac{1}{L} - \omega^2(C' + C_{f1}) + \frac{j\omega C_{f2}}{1 - \omega^2 L_{post} C_{f2}} = 0 \tag{5}$$

It is difficult to obtain the rest capacitance C' using analytical formulas. The fundamental and higher modes of the SRSIW cavity are investigated using the eigenmode in the full wave simulation software HFSS.

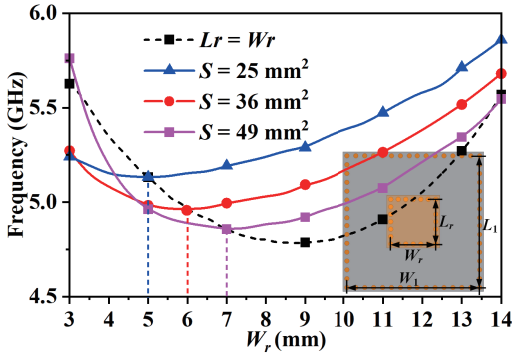

FIGURE 5. Corresponding resonant frequency of TE_{101} mode with different W_r. The inset represents a standard square SRSIW cavity. Dimensions in mm: $L_1 = W_1 = 16.8$, $L_r = W_r = 5.7$.

The electric field distribution of the fundamental mode in the SRSIW cavity is described in Fig. 4. It can be observed that the electric field is primarily distributed between the metal patch and upper metal plate, while the magnetic field is mainly concentrated near the central metal pillar array. Fig. 5 depicts the corresponding resonant frequency of TE_{101} mode with different values of W_r in the SRSIW cavity. As the area of the ridge increases, the C_{f1} becomes larger while the L_{post} becomes smaller. When the increased capacitance dominates, the resonant frequency of the SRSIW cavity decreases as W_r increases in the region $L_r = W_r \in [3, 9.8]$. In contrast, the resonant frequency of the SRSIW cavity increases as W_r increases in the region $L_r = W_r \in [9.8, 14]$ when the reduced inductance dominates. As a result, there is an optimal size for the ridge that maximizes the level of miniaturization of the SRSIW. The area of the ridge is defined as $S = L_r \times W_r$. When the area of the ridge is fixed as a constant, C_{f1} reaches its maximum value only as $L_r = W_r$. In addition, the perimeter of the ridge is minimized when $W_r = L_r$, which means that there is a minimum number of the metallized through holes connecting the patch to ground, then L_{post} reaches its maximum value at this point, and the resonant frequency of the SRSIW cavity is minimized. The level of miniaturization is maximized when the area of ridge is fixed, and its aspect ratio equals that of the SRSIW cavity.

2.3. Analysis of Loading Triple-Ridge SIW Cavity

A loading triple-ridge SIW (TRSIW) cavity with L_1 two times of W_1 is proposed. Figs. 6(a) and (b) represent the electric

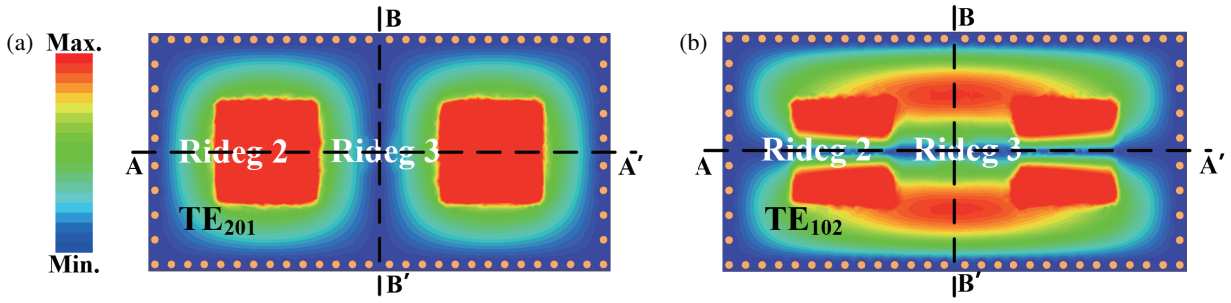

FIGURE 6. Electric field distribution of the center rectangular TRSIW cavity with aspect ratio of 2. (a) TE_{201} mode. (b) TE_{102} mode.

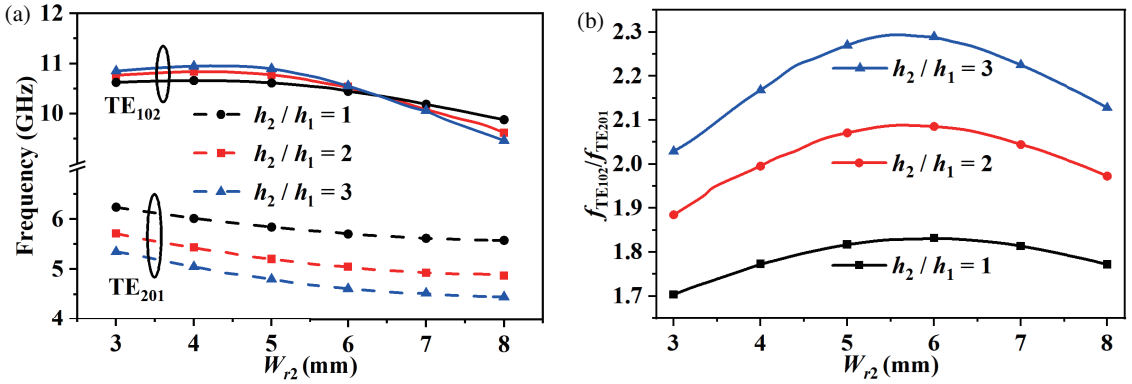

FIGURE 7. (a) Corresponding resonant frequencies of TE_{102} and TE_{201} modes versus W_{r2} and h_2/h_1 in the TRSIW cavity. (b) f_{TE102}/f_{TE201} versus W_{r2} and h_2/h_1 in the TRSIW cavity.

field distribution of the orthogonal degenerate TE_{201} and TE_{102} modes in the TRSIW cavity, respectively. It can be observed that along the central symmetric plane A-A′, the electric field of TE_{201} mode is always the strongest, while the TE_{102} mode is the weakest. On the contrary, the electric field is the strongest for TE_{102} and the weakest for TE_{201} mode along the central symmetrical plane B-B′. Based on the above properties, cross-transmission with appropriate interchannel isolation can be achieved if four feeding ports are placed along A-A′ and B-B′ to excite this TRSIW cavity. The value of f_{TE102}/f_{TE201} can be further increased for a certain L_1/W_1 with the technique of loading ridge. In this way, the resonant frequency of the TE_{201} mode is able to be minimized due to the loading of the ridges at the location in the SIW cavity where the TE_{201} mode electric field is the strongest. However, the ridges are located away from the strongest position of the electric field of the TE_{102} mode, and then the influence of the ridges on the f_{TE102} is alleviated.

From Fig. 7(a), it can be clearly observed that the value of f_{TE201} decreases significantly as h_2/h_1 increases. This is because the parasitic capacitance increases for the TE_{201} mode when the h_2/h_1 becomes larger. However, the electric field is partly concentrated between the patch and the top metal for the TE_{102} mode. The electric field variation is not significant when h_2/h_1 increases, thus resulting in minimal changes to f_{TE102}. Consequently, the value of f_{TE102}/f_{TE201} increases as h_2/h_1 increases. As W_{r2} increases, the parasitic capacitance increases for TE_{201} and TE_{102} modes, which results in the decrease of resonant frequencies of both TE_{102} and TE_{201} modes.

Figure 7(b) shows that there is a suitable value of $W_{r2}(W_{rs})$, which maximizes f_{TE102}/f_{TE201} when h_2/h_1 is fixed. There is a positive correlation between f_{TE102}/f_{TE201} and W_{r2} in the region $W_{r2} \in [3, W_{rs}]$. When $W_{r2} > W_{rs}$, there is a negative correlation between f_{TE102}/f_{TE201} and W_{r2}. The value of f_{TE102}/f_{TE201} reaches the maximum value (2.09) when $W_{r2} = 5.7$ mm and $h_2/h_1 = 2$.

2.4. Design of Proposed Filtering Crossover

The coupling coefficients k_{12} and k_{45} for various values of W_{m1} and W_{m2} are plotted in Figs. 8(a) and (b), which are extracted by ANSYS HFSS. It is evident that k_{12} and k_{45} become larger with the increase of W_{m1} and W_{m2}. The bandwidths of the two channels can be allocated flexibly by adjusting W_{m1} and W_{m2}. Figs. 9(a) and (b) show external Q-factor of Ch. I by varying L_{s1}, L_{s2}, and W_{s1}. Fig. 9(c) depicts the external Q-factor of Ch. II by varying L_{s3} and W_{s3}. The Q-factor of Ch. I and Ch. II increases by enlarging length and width of their corresponding slot gap.

As analyzed above, the key design steps are described as follows. From Fig. 7, the thickness ratio h_2/h_1 of the substrates and the TRSIW resonator's initial dimensional parameters can be determined according to the desired frequency ratio range of two paths. Furthermore, the increase of W_{m1} and W_{m2} can be used to obtain wider bandwidth according to Fig. 8.

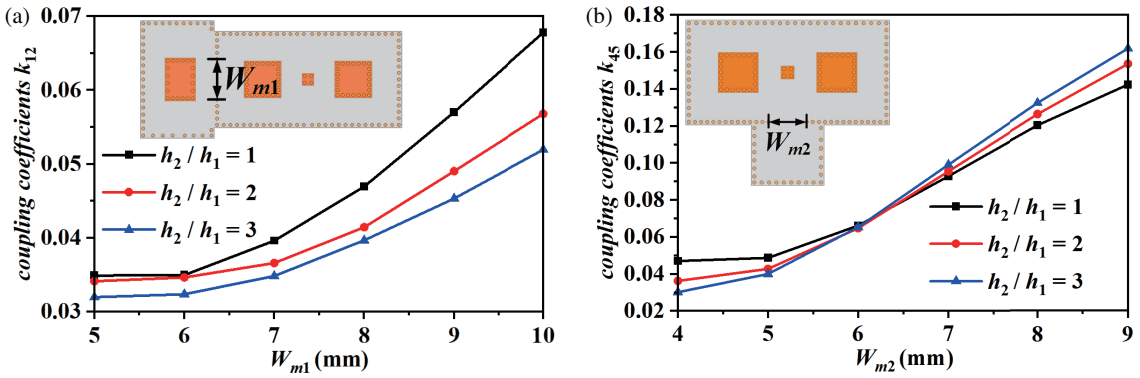

FIGURE 8. Coupling coefficients (a) k_{12} as a function of W_{m1} and (b) k_{45} as a function of W_{m2}.

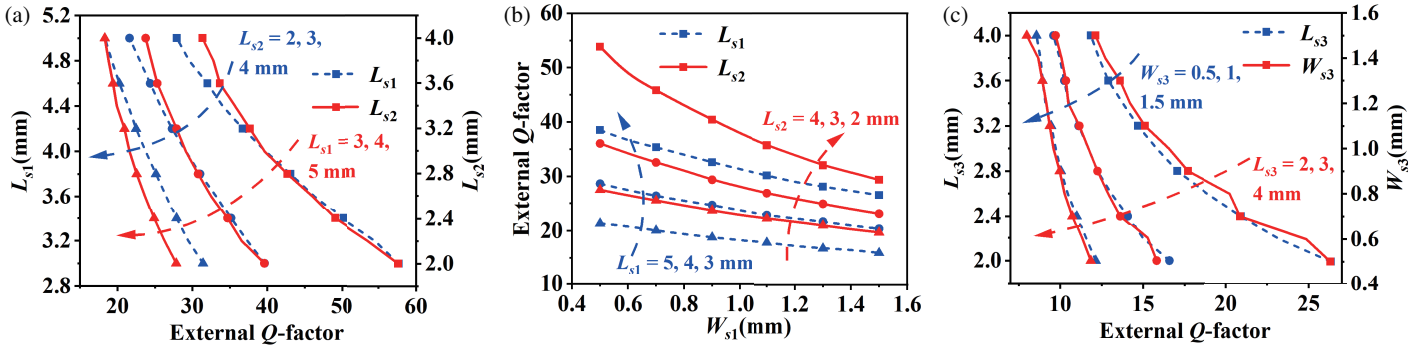

FIGURE 9. (a) External Q-factor of Ch. I by varying L_{s1} and L_{s2}. (b) External Q-factor of Ch. I by varying L_{s1}, L_{s2} and W_{s1}. (c) External Q-factor of Ch. II by varying L_{s3} and W_{s3}.

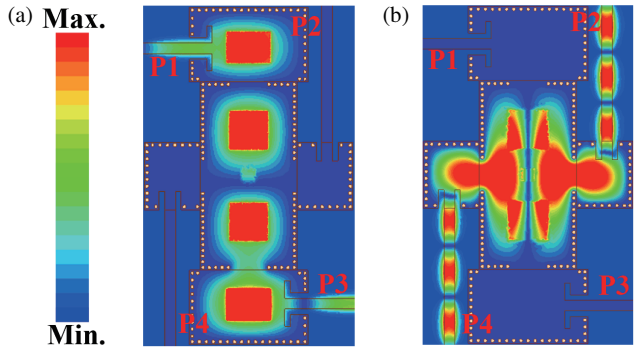

FIGURE 10. Electric field distributions of the two intersecting channels for the proposed RSIW filtering crossover with different channel CFs. (a) Excitation of port P1 (5 GHz). (b) Excitation of port P2 (10.1 GHz).

To elaborate the operating mechanism of the filtering crossover more intuitively, Fig. 10 depicts the electric field magnitude distributions of the proposed RSIW filtering crossover. When port P1 is driven, it is obvious that TE_{101} is excited in cavities 1 and 3, and TE_{201} is excited in cavity 2, which constructs the longitudinal channel from port P1 to port P3. Besides, little energy leaks into adjacent channels when P1 is excited. When driving port P2, energy will only be transferred from port P2 to port P4 with high isolation from ports P1 and P3.

Figure 11 illustrates the simulated S-parameters of the proposed RSIW filtering crossover with and without ridge 3. It is obvious that f_{TE101} is close to the first passband and f_{TE301} close to the second passband when the center TRSIW cavity lacks ridge 3, which can easily cause undesired spurious passbands. The resonant frequencies of TE_{301} and TE_{101} can be appropriately lowered and moved away from the passband by loading ridge 3. As a result, a good rejection level between the two passbands can be achieved.

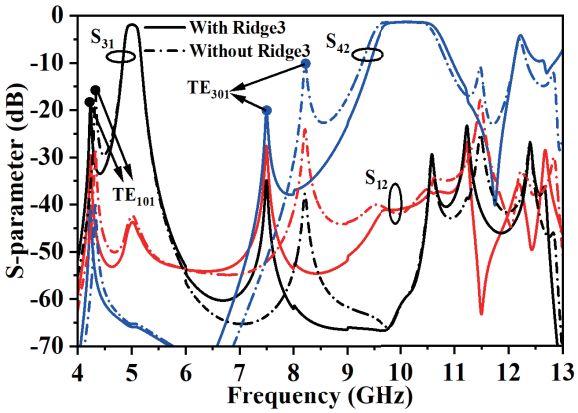

FIGURE 11. Simulated S-parameters of the proposed RSIW filtering crossover with and without ridge 3.

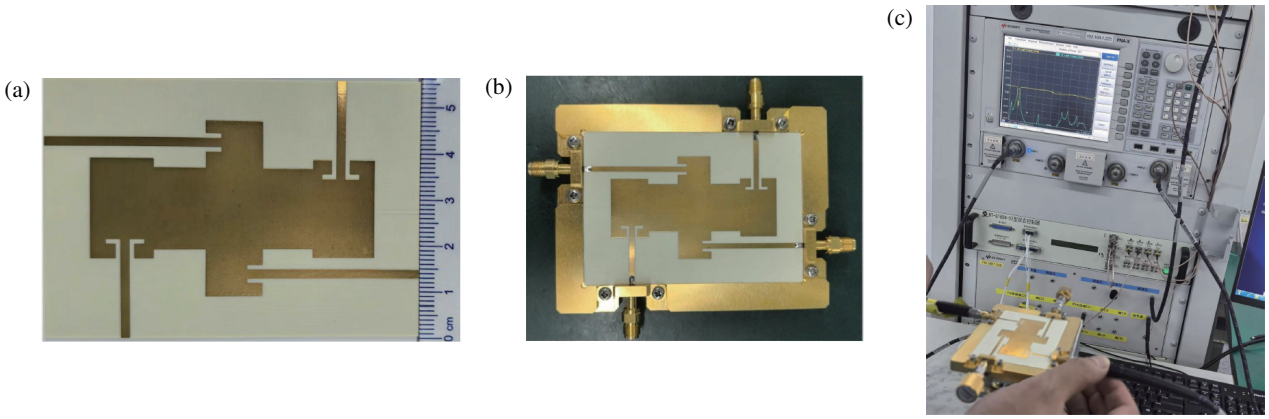

FIGURE 12. (a) The photograph of the fabricated prototype. (b) The proposed filtering crossover test model. (c) Measurement setup using Keysight N5244A vector network analyzer (VNA).

3. MEASUREMENT AND RESULTS

3.1. Experimental Setup and Preparation

To verify the practicality of the proposed structure, an RSIW filtering crossover sample is fabricated as shown in Fig. 12(a). The size of the sample is 60.46 mm × 37.5 mm ($1.88\lambda g \times 1.17\lambda g$, and λg is the waveguide wavelength at the CF of the first passband). The final dimensions are: $L_1 = 32.8$, $W_1 = 16.4$, $L_2 = 12.33$, $W_2 = 20.25$, $L_3 = 11.06$, $W_3 = 9.05$, $L_{s1} = 4.12$, $L_{s2} = 3.12$, $L_{s3} = 3.3$, $W_{s3} = W_{s3} = W_{s3} = 1$, $W_{m1} = 7.3$, $W_{m2} = 6.3$, $L_{r1} = 4.5$, $W_{r1} = 6.81$, $L_{r2} = W_{r2} = 5.7$, $L_{r3} = W_{r3} = 1.2$, $W_t = 1.9$ (unit: mm). Fig. 12(b) shows a picture of the filtering crossover test model. The entire test tool is connected to the outer conductor of the Sub-Miniature Push-on (SMP) connector and thus grounded. The fabricated prototype was measured using Keysight N5244A vector network analyzer (VNA) as shown in Fig. 12(c). Connect the SMP connector to the Keysight N5244A VNA by using the SMP to Sub-Miniature version A (SMA) conversion connector.

3.2. Measurement Results and Discussion

Figure 13 shows the simulated and measured S-parameters of the RSIW filtering crossover. The measured CFs are 4.98 GHz and 10.1 GHz within a 20 dB return loss fractional bandwidth (FBW) of 3.20% and 7.1% (3-dB FBW of 5.20% and 10.8%),

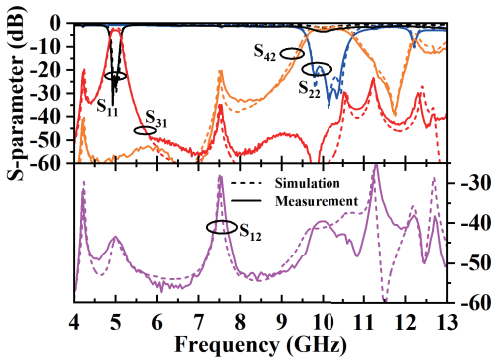

FIGURE 13. Simulated and measured results of the proposed RSIW filtering crossover. The inset is the photograph of the fabricated prototype.

TABLE 1. Comparison with other works.

Reference	[7]	[8]	[9]	[10]	This work
CF (GHz)	8.0/8.82	7.37/8.78	12/13.5	5.8/27	4.98/10.1
3dB-FBW(%)	5.0/4.5	4.47/3.3	6.92/6.07	1.9/2.3	5.20/10.8
IL (dB)	1.75/1.44	2.3/2.13	1.23/1.42	0.9/0.7	2.93/2.42
RL (dB)	20/25	15.4/15.4	16.2/14.0	10/15	20/20
Iso. (dB)	> 21	> 15.43	> 29	> 120	> 38.7
Size (λ_g^2)	3.98	2.11	5.47	0.44	2.20
Rejection	$\times$	$\times$	11	6.7	20
Tech.	SIW	SIW	SIW	Wave guide	SIW
Order	2	2	3	3	3

Iso.: Isolation; Tech.: Technology.

respectively. The simulated CFs are 5 GHz and 10.13 GHz within a 20 dB return loss FBW of 3.20% and 7.5% (3-dB FBW of 520% and 11.43%), respectively. For channel I, the measured CF is shifted by 0.4% from the simulated CF in the proposed filter. The measured and simulated FBWs are in good agreement in the proposed filter. For channel II, the measured CF is shifted by 0.3% from the simulated CF in the proposed filter. The measured FBW is 5.3% smaller than the simulated value of FBW in the proposed filter. Slight differences of CFs between simulated and measured results may be due to shifts in the dielectric constant of the substrate or processing tolerance. Especially, during the lamination process of the substrates, the thickness ratio of the substrates may change. From Fig. 8(c), it can be inferred that the narrowing of the FBW of channel II may be due to the actual size of w_{m2} being smaller than the simulated size.

The simulated minimum insertion loss (IL) in passband is 1.92 dB and 1.37 dB, and the measured minimum IL in passband is 2.93 dB and 2.42 dB, which includes losses of two SMP connectors and two SMP to SMA conversion connectors. Furthermore, a high isolation level greater than 38.71 dB within 20-dB return loss can be observed. The first spurious passband appears around 12.25 GHz, which is caused by the f_{TE302} of the center cavity close to the second passband. Although the simulation results differ from the measurements, the discrepancy is within acceptable limits. We can consider that the simulated and the measured results are in excellent agreement.

Table 1 lists the comparison of the proposed filtering crossover with previous similar works. Compared to [7–9], it can be clearly observed that the proposed structure shows a larger frequency ratio. Better isolation can be achieved due to the harmonic interleaving technique. The rejection level of the stopband is greater than the design in [10] without low-pass filter cascaded.

4. CONCLUSION

In this letter, an RSIW filtering crossover with a relatively large frequency ratio of 2.03 is designed. The frequency ratio of the two paths can be flexibly controlled by adjusting the aspect ratio of the center RSIW cavity and ridges loaded. In addition, the influence of loading ridge on the resonant frequency of RSIW cavity is explored. Higher isolation levels and rejection levels of the filtering crossover can be realized thanks to the application of the harmonic interleaving technique. A sample is designed, fabricated, and measured. Good consistency between simulation and measurement validates the application of beamforming networks of radar systems.

REFERENCES

[1] Liu, Q., H. Qian, D.-W. Zhang, K. Gong, and Q.-K. Liu, "Compact highly-selective bandpass filter based on triple-mode ridge substrate integrated waveguide cavity," *IEEE Microwave and Wireless Technology Letters*, Vol. 33, No. 9, 1274–1277, 2023.

[2] Zheng, Y., H. Tian, and Y. Dong, "Miniaturized, wide stopband filter based on shielded capacitively loaded SIW resonators," *Chinese Journal of Electronics*, Vol. 33, No. 2, 456–462, 2024.

[3] Zhou, K., C.-X. Zhou, and W. Wu, "Substrate-integrated waveguide dual-band filters with closely spaced passbands and flexibly allocated bandwidths," *IEEE Transactions on Components, Packaging and Manufacturing Technology*, Vol. 8, No. 3, 465–472, 2018.

[4] Han, S.-Q., K. Zhou, J.-D. Zhang, C.-X. Zhou, and W. Wu, "Novel substrate integrated waveguide filtering crossover using orthogonal degenerate modes," *IEEE Microwave and Wireless Components Letters*, Vol. 27, No. 9, 803–805, 2017.

[5] Zhou, Y., K. Zhou, J. Zhang, C. Zhou, and W. Wu, "Miniaturized substrate integrated waveguide filtering crossover," in *2017 IEEE Electrical Design of Advanced Packaging and Systems Symposium (EDAPS)*, 1–3, Haining, China, Dec. 2017.

[6] Zhang, G., X. Zhou, K.-D. Xu, J. Yang, X. Sun, B. Xu, K.-W. Tam, S. Feng, W. Tang, and J. Hong, "Design of wide-stopband and dual-band filtering crossovers based on mixed substrate integrated waveguide cavities," *IEEE Transactions on Microwave Theory and Techniques*, Vol. 71, No. 12, 5346–5357, 2023.

[7] Zhan, W.-L., J.-X. Xu, X.-L. Zhao, B.-J. Hu, and X. Y. Zhang, "Substrate integrated waveguide multi-channel filtering crossover with extended channel number and controllable frequencies," *IEEE Transactions on Circuits and Systems II: Express Briefs*, Vol. 67, No. 12, 2858–2862, 2020.

[8] Qu, L., Y. Zhang, J. Liu, X. Bo, H. Jing, and Y. Fan, "Design of filtering crossover and diplexer on SIW quadruple-mode resonators in a single cavity," *IEEE Access*, Vol. 8, 176 789–176 796, 2020.

[9] Zhou, K. and K. Wu, "Wide-stopband substrate-integrated waveguide filtering crossovers with flexibly allocated channel frequencies and bandwidths," *IEEE Transactions on Microwave Theory and Techniques*, Vol. 69, No. 7, 3264–3274, 2021.

[10] Hu, C., Y. Li, and J. Wang, "A large-frequency-ratio multichannel bandpass filter based on structure-shared mode-composite air-filled cavity resonators," *IEEE Transactions on Microwave Theory and Techniques*, Vol. 72, No. 6, 3650–3661, 2024.

[11] Yang, S., J. Xu, Z. Yu, J. Zhou, and W. Hong, "A structure reuse method for realizing large frequency ratio dual-band multichannel integrated filters," *IEEE Transactions on Circuits and Systems II: Express Briefs*, Vol. 69, No. 4, 2101–2105, 2022.

[12] Wei, H. and F. Zhu, "A dual-band filtering crossover with large frequency ratio for microwave and millimeter-wave applications," *Microwave and Optical Technology Letters*, Vol. 65, No. 11, 2890–2896, 2023.

[13] Qiu, L.-L., Y. Guo, L. Zhu, Z.-A. Ouyang, S. Huang, and L. Deng, "Third-order filtering crossover using dual-mode resonator for high-isolated channels," *International Journal of Communication Systems*, Vol. 37, No. 2, e5639, 2024.

[14] Amari, S., U. Rosenberg, and J. Bornemann, "Adaptive synthesis and design of resonator filters with source/load-multiresonator coupling," *IEEE Transactions on Microwave Theory and Techniques*, Vol. 50, No. 8, 1969–1978, 2002.

[15] Hong, J. and M. J. Lancaster, *Microstrip Filters for RF/Microwave Applications*, John Wiley & Sons, 2004.